



g-C₃N₄/Bi₄O₅I₂ heterojunction with I₃[−]/I[−] redox mediator for enhanced photocatalytic CO₂ conversion

Yang Bai^a, Liquun Ye^{a,b,*}, Li Wang^b, Xian Shi^a, Pingquan Wang^a, Wei Bai^{a,c},
Po Keung Wong^d

^a School of Oil & Natural Gas Engineering, Southwest Petroleum University, Chengdu 610500, China

^b Key Laboratory of Ecological Security for Water Source Region of Mid-line Project of South-to-North Water Diversion of Henan Province, College of Chemistry and Pharmaceutical Engineering, Nanyang Normal University, Nanyang 473061, China

^c Chengdu Institute of Organic Chemistry, Chinese Academy of Sciences, Chengdu 610041, China

^d School of Life Sciences, The Chinese University of Hong Kong, Shatin, NT, Hong Kong, China

ARTICLE INFO

Article history:

Received 17 March 2016

Received in revised form 23 April 2016

Accepted 25 April 2016

Available online 27 April 2016

Keywords:

g-C₃N₄

Bi₄O₅I₂

I₃[−]/I[−]

Photocatalysis

CO₂ conversion

ABSTRACT

Heterojunction is an effectively construction to improve the photocatalytic activity due to the excellent photo-induced carrier separation efficiency. In this paper, g-C₃N₄/Bi₄O₅I₂ heterojunction was prepared and characterized by X-ray diffraction patterns (XRD), field emission scanning electron microscope (FESEM), transmission electron microscopy (TEM), UV–vis diffuse reflectance spectra (DRS) and X-ray photoelectron spectroscopy (XPS). The photocatalytic data showed that g-C₃N₄/Bi₄O₅I₂ heterojunction had higher activity than pure g-C₃N₄ and Bi₄O₅I₂. At an optimal ratio of 1.0 mol% (11.4 wt% of Bi₄O₅I₂), g-C₃N₄/Bi₄O₅I₂ photocatalyst showed the highest photocatalytic reduction activity for CO₂ conversion with 45.6 μmol h^{−1} g^{−1} CO generation. Photocurrent and electrochemical impedance (EIS) spectroscopy revealed that higher photo-induced carrier separation efficiency of g-C₃N₄/Bi₄O₅I₂. Z-scheme charge transfer mode was proved by I₃[−]/I[−] redox mediator existence and superoxide radical (O₂^{•−}) and hydroxyl radical (•OH) quantification experiments.

© 2016 Elsevier B.V. All rights reserved.

1. Introduction

Carbon dioxide (CO₂) is the main greenhouse gases due to the fossil fuel combustion [1,2]. In order to eliminate the rigorous ecological problem, Kyoto Protocol was passed in 1997 [3,4]. However, it only played a limited role because some reasons from the governments. Although many technologies such as landfill and adsorption were used to dispose CO₂, it cannot consume CO₂ essentially [5,6]. At present, photocatalytic technology has been studied widely for CO₂ conversion into solar fuels [7–9]. And so, photocatalysis has been considered as the greenest technology to solve greenhouse effect and energy crisis simultaneously [7–10]. We all know that the photocatalyst is the most important part of photocatalysis. So, many new photocatalysts beyond oxides, such as sulphides (CdS and ZnS) [11–13], elements (sulfur and phosphorus) [14,15], and polymers (g-C₃N₄ and polyimide) [16–18] semiconductors were studied to seek high activity visible light photocatalysts.

In past reports, bismuth oxyhalides (BiOX: X=Cl, Br, I) nanomaterials have been widely studied due to the excellent electrical, optical, and catalytic properties [19,20]. Recently, inorganic graphene-like BiOX were frequently used as photocatalysts with outstanding photocatalytic activities [21–23]. For instances, Zhang and our group reported BiOCl exhibited better photocatalytic performance than TiO₂ (P25, Degussa) for dyes degradation under UV light irradiation [24,25]. BiOBr and BiOI showed very high visible light photocatalytic activity for bacteria inactivation or nitric oxide remove [26–28]. So, BiOX has attracted more and more attention because of their appropriate band gaps and layer structure. However, BiOX usually cannot show effective photocatalytic reduction activity for the hydrogen generation and CO₂ conversion at neutral condition due to the lower position conduction band (CB) minimum [21].

Theoretical calculations indicated that the position of CB was mainly dependent by the Bi 6p of BiOX [29–31]. It implied that content adjustment of bismuth may be feasible to promote the CB position of BiOX. And more works have proved that the bismuth-rich strategy can enhance the photocatalytic reduction activity of BiOX [32–35]. For instances, bismuth-rich Bi_xO_yX_z (X=Cl, Br, I) photocatalysts displayed high photocatalytic activity for Cr (VI),

* Corresponding author at: School of Oil & Natural Gas Engineering, Southwest Petroleum University, Chengdu 610500, China.

E-mail address: yeliquun@163.com (L. Ye).

molecular oxygen, water and CO₂ reduction [32–34]. Recently, Xiao reported solvothermal method to prepare Bi₄O₅I₂ for photocatalytic degradation of 4-*tert*-butylphenol [35]. However, the photocatalytic CO₂ reduction of Bi₄O₅I₂ still was not reported.

In this paper, in order to enhance the activity for photocatalytic CO₂ conversion, g-C₃N₄/Bi₄O₅I₂ heterojunction was structured via complex precursor method. The photocatalytic results showed g-C₃N₄/Bi₄O₅I₂ outstanding photocatalytic activity for CO₂ conversion. And the superoxide radical (O₂^{•−}) and hydroxyl radical (•OH) quantification experiments, and I3d XPS spectra also confirmed the I₃[−]/I[−] redox mediator assisted Z-scheme. This finding suggested that bismuth-rich Bi_xO_yX_z composites photocatalysts have outstanding photocatalytic activity due to the in suit redox mediator.

2. Experimental

2.1. Materials

Urea, Bi(NO₃)₃·5H₂O, KI, glycerol, ethanol, nitroblue tetrazolium (NBT), terephthalic acid (TA) and NaOH were purchased from Sinopharm Chemical Reagent Co., Ltd. And they were of analytical reagent grade without further purification.

2.2. Synthesis

2.2.1. g-C₃N₄

g-C₃N₄ was synthesized according to the literature method [36].

2.2.2. Complex precursor

KI (2 mmol) was dissolved into 20 mL glycerol, and 2 mmol Bi(NO₃)₃·5H₂O was dissolved into another 20 mL glycerol. Then, KI solution was added into the Bi(NO₃)₃·5H₂O solution drop by drop with continuously stirring. The suspension was transferred into Teflon-lined stainless steel autoclaves (50 mL) and kept at 160 °C for 16 h. After reaction, the complex precursors precipitate was obtained by centrifugation, and then washed with ethanol. Finally, it was dried at 80 °C under air atmosphere.

2.2.3. Bi₄O₅I₂

Complex precursor (0.3 g) was dispersed in 100 mL deionized water. Then, Bi₄O₅I₂ sample was obtained via a simple hydrolytic process, and washed successively with deionized water. Finally, it was dried at 80 °C.

2.2.4. g-C₃N₄/Bi₄O₅I₂

g-C₃N₄ (100 mg) was dispersed into 100 mL deionized water, and different percentage (10, 20, 50 and 70%) of complex precursor was dispersed into above solution with 300 W high pressure xenon irradiation. And samples with different ratio of g-C₃N₄/Bi₄O₅I₂. The (g-C₃N₄/10-Bi₄O₅I₂, g-C₃N₄/20-Bi₄O₅I₂, g-C₃N₄/50-Bi₄O₅I₂, g-C₃N₄/70-Bi₄O₅I₂) were obtained after drying at 80 °C.

2.3. Characterization

X-ray diffraction patterns (XRD) of the samples recorded at room temperature, by a Bruker D8 advance X-ray diffractometer using Cu Kα radiation and 2θ scan rate of 6 min^{−1}. Diffraction patterns were taken over the 2θ range 5–70°. FESEM images were obtained by a Sigma Zeiss Field Emission Scanning Electron Microscope. Transmission electron microscopy (TEM) and high-resolution transmission electron microscopy (HRTEM) images were obtained by a JEOL JEM-2100F (RH) Field Emission Electron Microscope. X-ray photoelectron spectroscopy (XPS) measurements were carried out by Thermo Scientific ESCALAB 250XI X ray Photoelectron Spectrometer (Al Ka, 150 W, C1s 284.8 eV). UV–vis

diffuse reflectance spectra (DRS) were obtained using UV–vis spectra (Perkin Elmer, Lambda 650s, BaSO₄ as a reference). The infrared spectra were obtained using a Nicolet 5700 Fourier transform infrared (FT-IR) spectrometer with KBr as the reference.

2.4. Photocatalytic CO₂ conversion

The photocatalytic reduction of CO₂ was carried out in Labsolar-III AG closed gas system (Beijing Perfect light Technology Co., Ltd., China). 0.10 g of g-C₃N₄, Bi₄O₅I₂ and g-C₃N₄/Bi₄O₅I₂ samples were uniformly dispersed onto a glass sheet with an area of 28.26 cm², and then the glass sheet was put in a reaction cell (Pyrex glass). The volume of the reaction system was 350 mL. Prior to the light irradiation, the above system was thoroughly vacuum-treated to remove the air completely. Subsequently, 5 mL H₂SO₄ (4 M) was injected into the reactor to react with NaHCO₃ to achieve 1 atm CO₂ gas. After that, the reactor was irradiated from the top by a 300 W high pressure xenon lamp with 400 nm cutoff filter (PLS-SXE300, Beijing Perfect light Technology Co., Ltd China) maintaining the photoreaction temperature at 15 °C with DC-0506 low-temperature thermostat bath (Shanghai Sunny Hengping Scientific Instrument Co., Ltd China). At each time interval, about 0.15 mL of gas was taken from the reaction cell with subsequent qualitative analysis by GC9790II gas chromatography (GC, Zhejiang Fuli Analytical Instrument Co., Ltd China) equipped with a flame ionization detector (FID, GDX-502 columns) and a thermal conductivity detector (TCD, TDX-01 columns). The quantification of the production yield was based on a calibration curve. The outlet gases were determined to be O₂, CO, CH₄ CO₂, and few H₂.

2.5. Reactive oxygen species (ROS) quantification experiments

NBT (2.5 × 10^{−5} mol L^{−1}, exhibiting an absorption maximum at 259 nm) was used to determine the amount of photocatalytic O₂^{•−} generation. The production of O₂^{•−} was quantitatively analysed by detecting the concentration of NBT with Lambda 650s spectrophotometer. TA (5 × 10^{−4} mol L^{−1}, 2 × 10^{−3} mol L^{−1} NaOH solution), which reacts readily with •OH to produce a highly fluorescent product, 2-hydroxyterephthalic acid fluorescence peak at about 425 nm by excitation with the wavelength of 315 nm), was employed as a probe molecule to determine the amount of photocatalytic •OH generation. The production of •OH was quantitatively analysed by detecting the concentration of 2-hydroxyterephthalic acid with Shimadzu fluorescence spectrophotometer (RF-5301pc) after centrifugation [37,38].

2.6. Photoelectrochemical measurement

The Mott–Schottky plots, transient photocurrent responses and electrochemical impedance spectra (EIS) of the samples were determined using a CHI660D electrochemical working station (CHI Instruments, Shanghai, China) in a three-electrode quartz cell with Na₂SO₄ (0.1 M) electrolyte solution. Samples was deposited on a fluorinated-tin-oxide (FTO) conducting glass as the working electrode. Ag/AgCl and Pt were used as the reference and the counter electrodes, respectively.

3. Results and discussion

Fig. 1 showed that XRD patterns of Bi₄O₅I₂, g-C₃N₄ and g-C₃N₄/20-Bi₄O₅I₂. For Bi₄O₅I₂, it can be seen that the XRD pattern was in agreement with is in agreement with previous reported results [35]. Based on its CIF file, the crystal structure of Bi₄O₅I₂ was showed in Fig. S1. And it is monoclinic structure, space group: P21, unit cell parameters: a = 1.494 nm, b = 0.5698 nm, and c = 1.126 nm, α = γ = 90.0°, β = 99.8°. The two mainly peaks at 28.8° and 31.5°

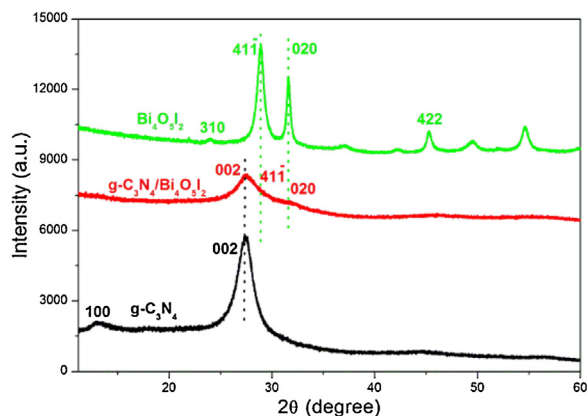


Fig. 1. XRD patterns of $\text{Bi}_4\text{O}_5\text{I}_2$, $\text{g-C}_3\text{N}_4$ and $\text{g-C}_3\text{N}_4/20\text{-Bi}_4\text{O}_5\text{I}_2$.

matched well with the (41-1) and (020) crystal planes of $\text{Bi}_4\text{O}_5\text{I}_2$. For pure $\text{g-C}_3\text{N}_4$, The two peaks at 13.0° and 27.4° were attributed to the (100) and (002) crystal planes of graphitic carbon nitride [16,17]. After $\text{Bi}_4\text{O}_5\text{I}_2$ was loaded on the surface of $\text{g-C}_3\text{N}_4$, the XRD pattern showed the main peak of $\text{g-C}_3\text{N}_4$ at 27.4° . However, the main peak of $\text{Bi}_4\text{O}_5\text{I}_2$ were emerged slightly at 28.8° and 31.5° . It should be due to the low content of $\text{Bi}_4\text{O}_5\text{I}_2$ in $\text{g-C}_3\text{N}_4/20\text{-Bi}_4\text{O}_5\text{I}_2$ photocatalyst. FT-IR spectrum (Fig. S2) showed that The intense bands in the $900\text{--}1200\text{ cm}^{-1}$ region can be assigned to the typical stretching modes of CN heterocyclic [17,18]. For pure $\text{Bi}_4\text{O}_5\text{I}_2$, the series of peaks at 541 and 634 cm^{-1} were attributed to the stretching vibrations of the Bi–O [39,40]. In $\text{g-C}_3\text{N}_4/\text{Bi}_4\text{O}_5\text{I}_2$, the spectra exhibited the characteristic peaks of both $\text{g-C}_3\text{N}_4$ and $\text{Bi}_4\text{O}_5\text{I}_2$, indicating the successful combination of the two components. In order to confirm the $\text{Bi}_4\text{O}_5\text{I}_2$ content, X ray photoelectron spectrometer was used to analyse the mole ratio of Bi/N.

Fig. 2 were the XPS spectra of $\text{Bi}_4\text{O}_5\text{I}_2$, $\text{g-C}_3\text{N}_4$ and $\text{g-C}_3\text{N}_4/20\text{-Bi}_4\text{O}_5\text{I}_2$. As shown in Fig. 2a, the survey spectrum implied that the $\text{g-C}_3\text{N}_4/20\text{-Bi}_4\text{O}_5\text{I}_2$ consisted of C, N, Bi, O, and I elements. And the

Bi/N mole ratio of $\text{g-C}_3\text{N}_4/20\text{-Bi}_4\text{O}_5\text{I}_2$ was 0.5/49.5. Therefore, it was 1.0 mol% (11.4 wt%) $\text{Bi}_4\text{O}_5\text{I}_2$ on the surface of $\text{g-C}_3\text{N}_4/20\text{-Bi}_4\text{O}_5\text{I}_2$. This data was in agreement with the above XRD result. On the other hand, the high-resolution XPS spectra of C1s (Fig. 2b) and N1s (Fig. 2c) also revealed the same binding energy and same intensity for $\text{g-C}_3\text{N}_4$ and $\text{g-C}_3\text{N}_4/20\text{-Bi}_4\text{O}_5\text{I}_2$. It also indicated that the content of $\text{Bi}_4\text{O}_5\text{I}_2$ was low in $\text{g-C}_3\text{N}_4/20\text{-Bi}_4\text{O}_5\text{I}_2$. The first C1s peak at 284.6 eV corresponded to carbon impurities which was usually observed in the XPS analysis and used as the calibration peak. The second (288.1 eV) and weakest C1s (293.4 eV) peaks were identified as sp^2 -bonded carbon (N-C=N) and the π -excitations of CN heterocycles, respectively [16,17,36]. The first (398.57 eV), second (400.0 eV), third (401.27 eV) and weakest (404.36 eV) N1s peaks were corresponded to the sp^2 hybridized aromatic N bonded to carbon atoms (C-N=C), the tertiary N bonded to carbon atoms in the aromatic cycles, and the π -excitations of CN heterocycles, respectively [16,17,36]. Fig. 2d displayed the high-resolution XPS of Bi4f. Firstly, the intensity of $\text{g-C}_3\text{N}_4/20\text{-Bi}_4\text{O}_5\text{I}_2$ was much lower than that of $\text{Bi}_4\text{O}_5\text{I}_2$, which verified the above conclusion about Bi/N mole ratio. Furthermore, compared to pure $\text{Bi}_4\text{O}_5\text{I}_2$, the Bi4f XPS peaks of $\text{g-C}_3\text{N}_4/20\text{-Bi}_4\text{O}_5\text{I}_2$ increased 0.46 and 0.36 eV for Bi4f 7/2 and Bi4f 5/2, respectively. And the full-width at half-maximum (FWHM) of Bi4f 7/2 increased significantly from 1.11 eV to 1.32 eV . The peak shifts and broadening implied the binding interaction between $\text{Bi}_4\text{O}_5\text{I}_2$ and $\text{g-C}_3\text{N}_4$ that during the hydrolytic process [41].

Fig. 3 showed the comparison of the UV–vis DRS spectra of $\text{Bi}_4\text{O}_5\text{I}_2$, $\text{g-C}_3\text{N}_4$ and $\text{g-C}_3\text{N}_4/20\text{-Bi}_4\text{O}_5\text{I}_2$. The $\text{Bi}_4\text{O}_5\text{I}_2$ and $\text{g-C}_3\text{N}_4$ had fundamental absorption edges at 570 nm and 450 nm , respectively. After $\text{Bi}_4\text{O}_5\text{I}_2$ loading on the surface of $\text{g-C}_3\text{N}_4$, the $\text{g-C}_3\text{N}_4/20\text{-Bi}_4\text{O}_5\text{I}_2$ showed the absorption edge at 454 nm . The corresponding band gap values of $\text{Bi}_4\text{O}_5\text{I}_2$ (2.19 eV), $\text{g-C}_3\text{N}_4$ (2.76 eV) and $\text{g-C}_3\text{N}_4/20\text{-Bi}_4\text{O}_5\text{I}_2$ (2.73 eV) were compared as shown in Fig. 3b [36]. It indicated that all samples can be excited by visible light ($\lambda > 400\text{ nm}$) irradiation.

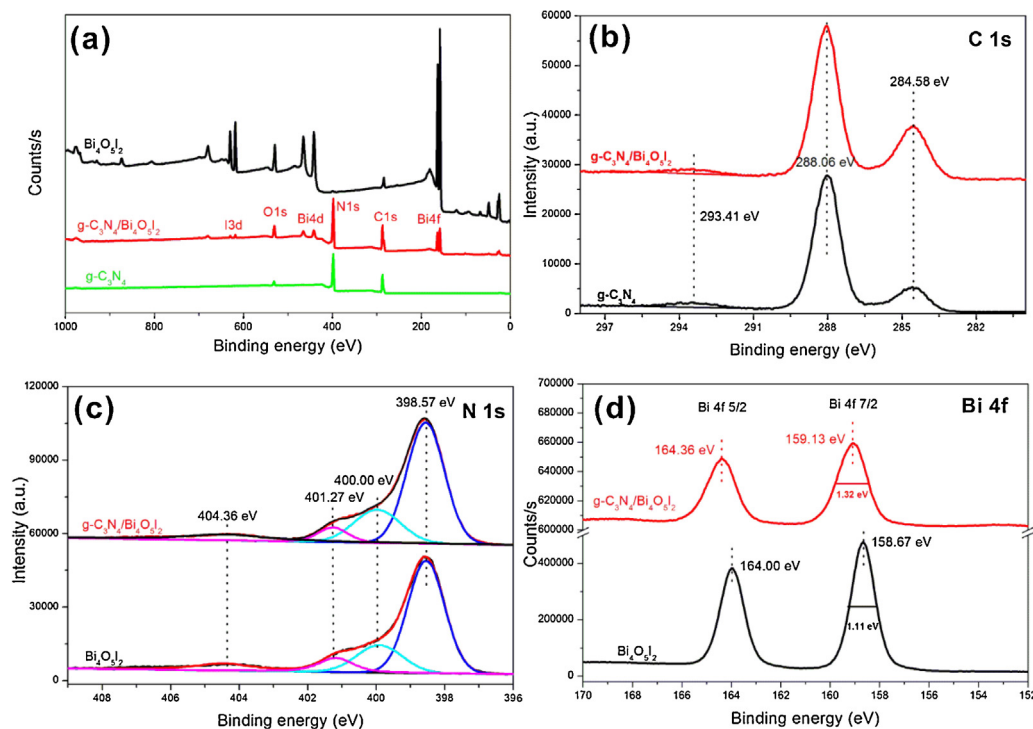


Fig. 2. XPS spectra of $\text{Bi}_4\text{O}_5\text{I}_2$, $\text{g-C}_3\text{N}_4$ and $\text{g-C}_3\text{N}_4/20\text{-Bi}_4\text{O}_5\text{I}_2$: (a) survey; (b) C 1s; (c) N 1s; and (d) Bi 4f.

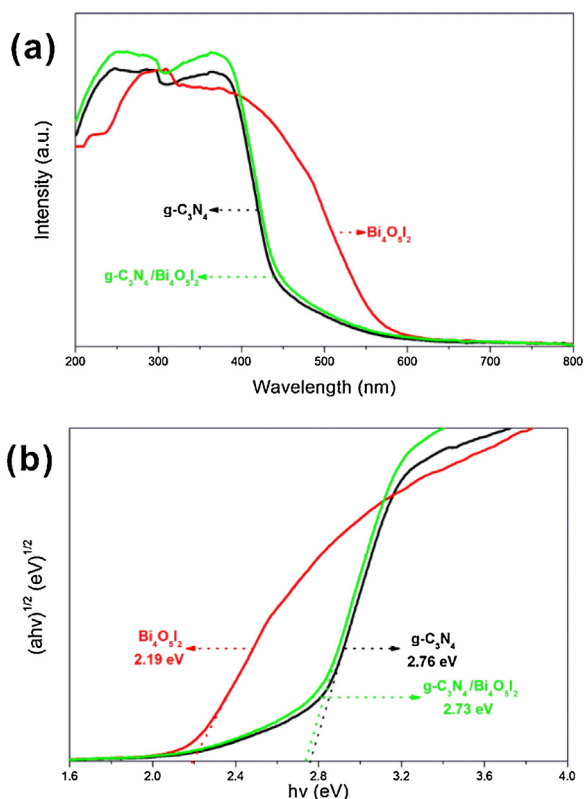


Fig. 3. DRS spectra of $Bi_4O_5I_2$, $g-C_3N_4$ and $g-C_3N_4/20-Bi_4O_5I_2$.

SEM, TEM and HRTEM images of $g-C_3N_4/20-Bi_4O_5I_2$ were showed in Fig. 4. SEM displayed that the main part of $g-C_3N_4/20-Bi_4O_5I_2$ were $g-C_3N_4$ rather than $Bi_4O_5I_2$. And Fig. 4b revealed the small $Bi_4O_5I_2$ nanoparticles (red zone) were loading on the surface of $g-C_3N_4$. TEM image also revealed the same results with SEM. The size of $Bi_4O_5I_2$ nanoparticles were about 20 nm (Fig. S3), which much smaller than pure $Bi_4O_5I_2$ (Fig. S4). HRTEM image showed a clear lattice spacing of 0.31 nm was indexed to the {41-1} facets of $Bi_4O_5I_2$.

Photocatalytic CO_2 conversion was a new application for bismuth oxyhalides photocatalysts. In past two years, our group studied the CO_2 conversion into solar fuels over $BiOBr$, $BiOI$, Bi_5O_7I , and $Bi_4O_5I_2$ [34,42]. And we also found that $Bi_4O_5I_2$ displayed outstanding photocatalytic activity for CO_2 conversion under visible light irradiation. Here, after $Bi_4O_5I_2$ loading on the surface of $g-C_3N_4$, we look forward to enhanced activity for $Bi_4O_5I_2$. Fig. 5a was the photocatalytic rates of products for CO_2 conversion over $g-C_3N_4/x-Bi_4O_5I_2$ ($x=0, 10, 20, 50, 70$, and 100) under visible light irradiation for 5 h. It can be seen that there are CO , CH_4 , O_2 and H_2 were generated in $g-C_3N_4/x-Bi_4O_5I_2$ system for CO_2 conversion, and CO was the uppermost product. The best one was $g-C_3N_4/x-Bi_4O_5I_2$ photocatalyst with $45.6 \mu mol h^{-1} g^{-1}$, which was about 7.9 times than that of pure $g-C_3N_4$ ($5.8 \mu mol h^{-1} g^{-1}$) and 2.3 times than that of pure $Bi_4O_5I_2$ ($19.8 \mu mol h^{-1} g^{-1}$). To the best of our knowledge, as shown in Table S1, this CO generation rate of $g-C_3N_4/20-Bi_4O_5I_2$ was the highest on of all reported Bi-O-X photocatalysts. Fig. 5b displayed the photocatalytic yields of $g-C_3N_4/20-Bi_4O_5I_2$ under visible light irradiation for different time. As can be seen, the total yields of CO , CH_4 , O_2 and H_2 were enhanced with the irradiation time continuation. It indicated that $g-C_3N_4/Bi_4O_5I_2$ samples can used for CO_2 photoreduction for the whole time. And the cyclic experiment (Fig. 5c) also revealed that the reduction of the photocatalytic activity was about 10% after 5 cycles (5 h per cycle). The fifth photocatalytic rate ($40.5 \mu mol h^{-1} g^{-1}$) still was about 6.89 times than that of pure $g-C_3N_4$ ($5.8 \mu mol h^{-1} g^{-1}$) and 2.0 times than that of pure $Bi_4O_5I_2$ ($19.8 \mu mol h^{-1} g^{-1}$).

As we know that the photocatalytic activity usually affected by the photon absorption efficiency, photo-induced carrier separation efficiency, adsorption, hydrophilicity, and so on. Based on the above DRS spectra, the photon absorption efficiency of $g-C_3N_4/20-Bi_4O_5I_2$, $Bi_4O_5I_2$ and $g-C_3N_4$ should be at the same level. So, the photocatalytic activity enhancement should come from the improved photo-induced carrier separation efficiency. For proving this pinot, the electrochemical impedance and photocurrent responses spectra of $Bi_4O_5I_2$, $g-C_3N_4$ and $g-C_3N_4/20-Bi_4O_5I_2$ were compared as shown in Fig. 6. It was observed that the smaller diameter of semicircle arc of $g-C_3N_4/20-Bi_4O_5I_2$ than that of pure $g-C_3N_4$ and pure $Bi_4O_5I_2$. Furthermore, the diameter of semicircle arc of all

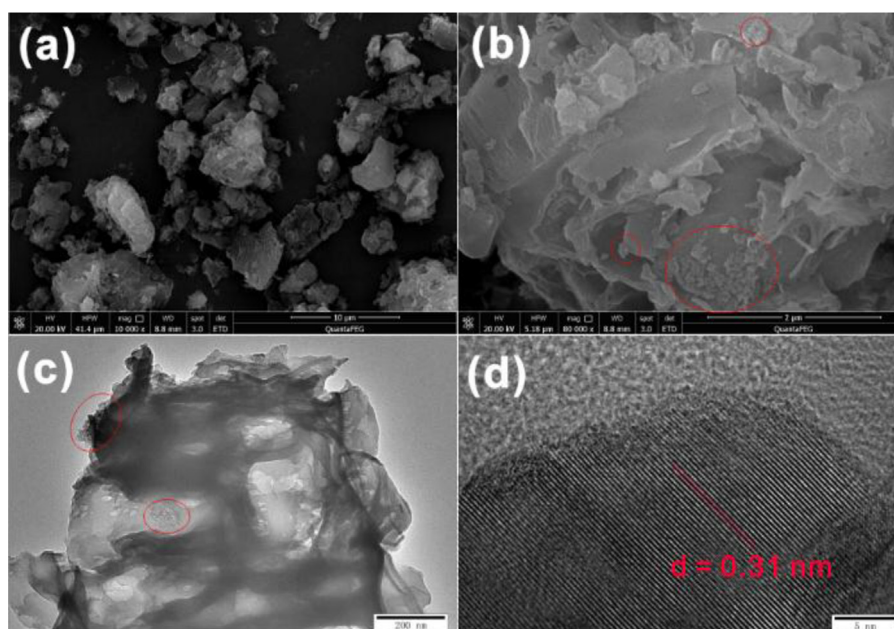


Fig. 4. SEM, TEM and HRTEM images of $g-C_3N_4/20-Bi_4O_5I_2$.

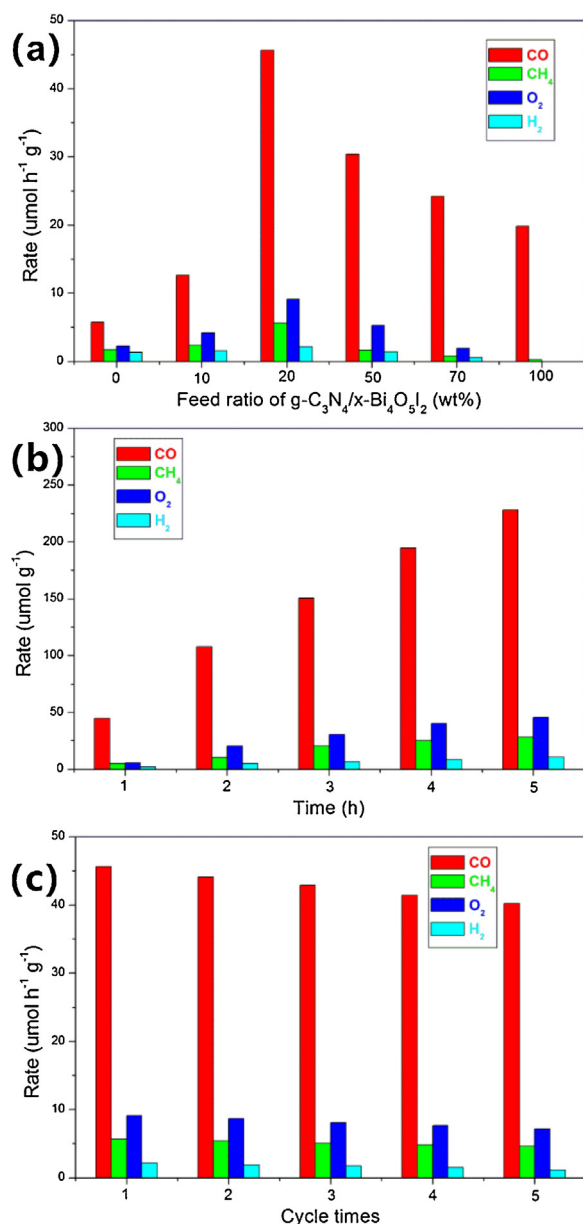


Fig. 5. (a) Rates of products for g-C₃N₄/x-Bi₄O₅I₂ (x=0, 10, 20, 50, 70, and 100) under visible light irradiation for 5 h, (b) yields of the products over g-C₃N₄/20-Bi₄O₅I₂ under visible light irradiation for different time, and (c) cyclic experiment over g-C₃N₄/20-Bi₄O₅I₂ under visible light irradiation for 5 h per circulation.

samples with light on were smaller than that of light off (in dark). It revealed that g-C₃N₄/Bi₄O₅I₂ had a lower electron-transfer resistance value (Fig. 6a) than that of g-C₃N₄ and pure Bi₄O₅I₂, especially when light on. On the other hand, the photocurrent for g-C₃N₄/20-Bi₄O₅I₂ was much higher than that of pure g-C₃N₄ and pure Bi₄O₅I₂ when light was on (Fig. 6b). Therefore, the mobility and separation efficiency of the photo-induced carriers was efficaciously improved after Bi₄O₅I₂ loading on the surface of g-C₃N₄.

In order to understand the photo-induced carrier separation mechanism, the energy band structure including band gaps, conduction band (CB) and valence band (VB) positions of pure Bi₄O₅I₂ and g-C₃N₄ should be confirmed. The Mott–Schottky plots of pure g-C₃N₄ (Fig. 7a) and Bi₄O₅I₂ (Fig. 7b) film electrodes at frequencies of 1000 and 2000 Hz were showed. The flat potentials of g-C₃N₄ and Bi₄O₅I₂ were calculated to be −0.55 and −0.24 V versus the Ag/AgCl electrode, respectively. And they were equivalent to −0.23 and −0.02 V versus the normal hydrogen electrode (NHE) [43,44].

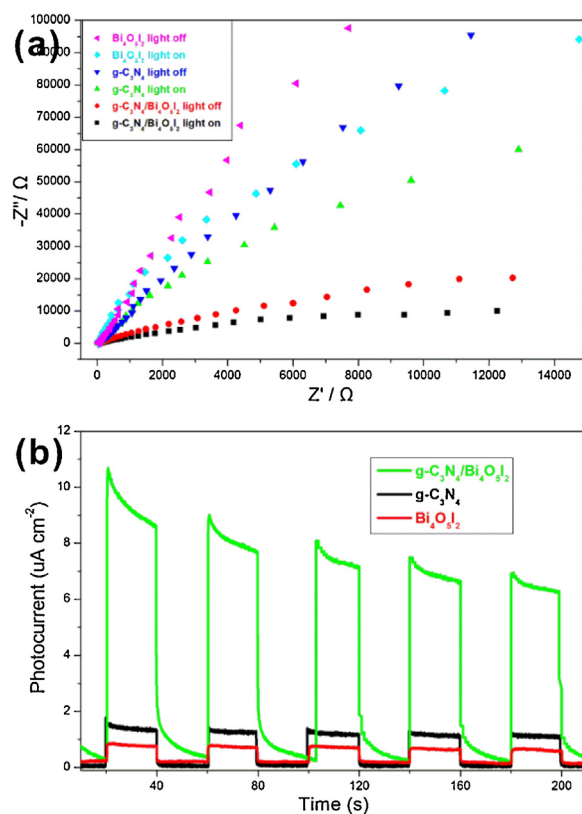


Fig. 6. (a) electrochemical impedance and (b) photocurrent responses spectra of Bi₄O₅I₂, g-C₃N₄ and g-C₃N₄/20-Bi₄O₅I₂.

Fig. 7c was the VB-XPS spectra of g-C₃N₄ and Bi₄O₅I₂. It showed that the energy gap between the valence band of Fermi level (E_{vf}) were 2.31 and 1.45 eV for pure g-C₃N₄ and Bi₄O₅I₂, respectively [45]. It is known that the flat potentials of n-type semiconductors was the fermi level [45–47]. So, the VB positions of g-C₃N₄ and Bi₄O₅I₂ were 2.08 and 1.45 eV, respectively. Based on the band gaps, the CB positions of g-C₃N₄ and Bi₄O₅I₂ were −0.68 and −0.76 eV, respectively. And the diagram of the band energy of Bi₄O₅I₂ and g-C₃N₄ was showed in Fig. 7d.

It can be found that the band energies of Bi₄O₅I₂ and g-C₃N₄ (Fig. 7d) were matching for charge transfer mechanism to improve photo-induced carrier separation efficiency. However, we also found that the E_{vf} of g-C₃N₄ was higher than Bi₄O₅I₂. It implied Z-scheme mechanism also suitable for photo-induced carrier separation efficiency enhancement [45]. In order to check which mechanism happened, ROS quantification experiments were showed in Fig. 8. By comparing the change of ROS concentration, it can confirm the photocatalytic oxidation reaction and reduction reaction happening positions of g-C₃N₄/Bi₄O₅I₂. For photocatalytic reduction reaction, NBT was used to test $\text{O}_2^{\bullet-}$. It can be seen that g-C₃N₄ and Bi₄O₅I₂ display same reduction activity for $\text{O}_2^{\bullet-}$ generation due to the equilibration of CB potential and photo-induced carrier separation efficiency (higher CB potential and lower separation efficiency for Bi₄O₅I₂, lower CB potential and higher separation efficiency for g-C₃N₄). After Bi₄O₅I₂ loading, g-C₃N₄/Bi₄O₅I₂ displayed enhanced reduction activity for $\text{O}_2^{\bullet-}$ generation. Because charge transfer mechanism resulted g-C₃N₄-CB reduction position and Z-scheme mechanism resulted Bi₄O₅I₂-CB reduction position all can improve the reduction activity of g-C₃N₄/Bi₄O₅I₂, it is difficult to confirm which mechanism happened via photocatalytic reduction reaction. For photocatalytic oxidation reaction, TA was used to test $\cdot\text{OH}$. It can be seen that g-C₃N₄/Bi₄O₅I₂ displayed enhanced oxidation activity than pure g-C₃N₄. And Bi₄O₅I₂ did not

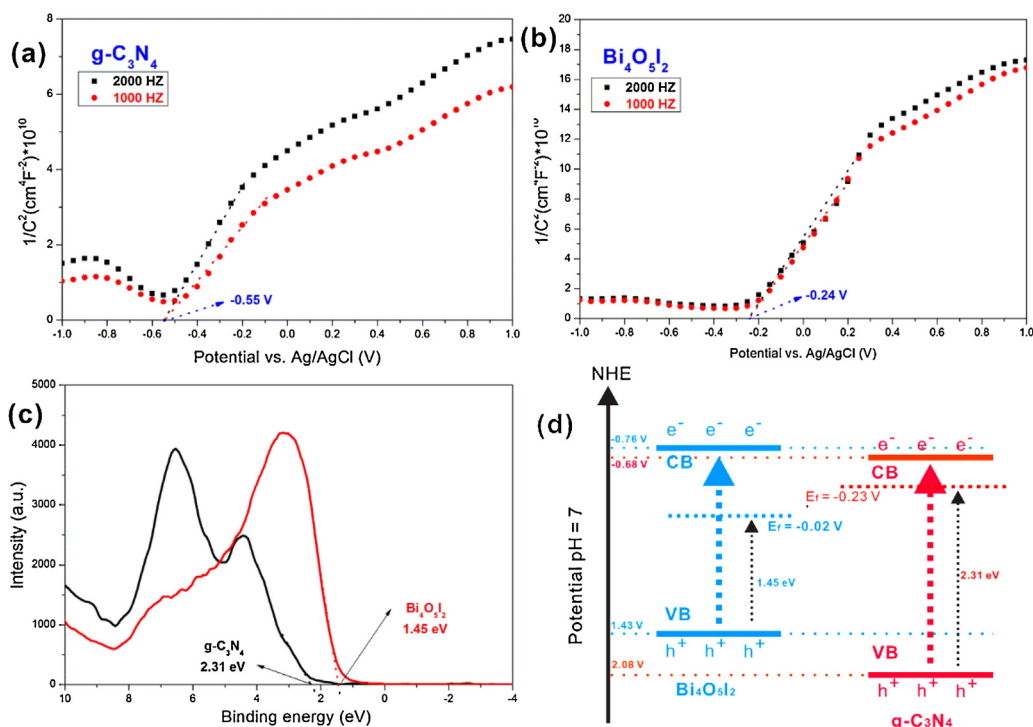


Fig. 7. Mott-Schottky plots of pure $g-C_3N_4$ (a) and $Bi_4O_5I_2$ (b) film electrodes at frequencies of 1000 and 2000 Hz in an aqueous solution of Na_2SO_4 (0.1 M); (c) valence band XPS spectra of pure $g-C_3N_4$ and $Bi_4O_5I_2$; and (d) Diagram of the band energy of $Bi_4O_5I_2$ and $g-C_3N_4$.

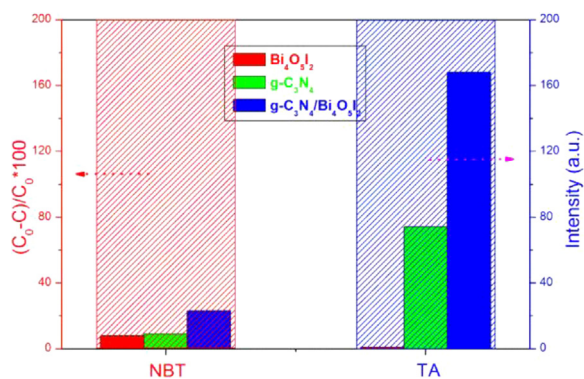


Fig. 8. Reactive oxygen species quantification experiments under visible light irradiation: NBT for $O_2^{\cdot -}$ and TA for $\cdot OH$.

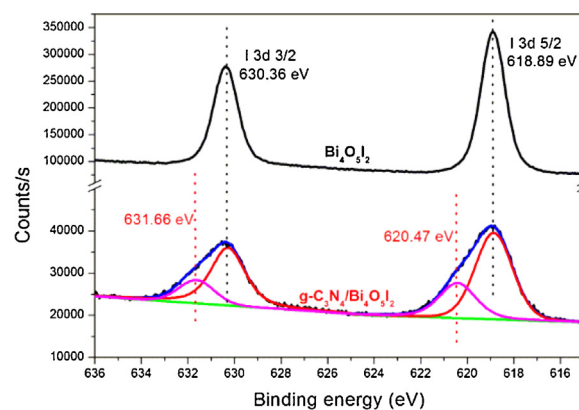


Fig. 9. I 3d XPS spectra of $Bi_4O_5I_2$ and $g-C_3N_4/20-Bi_4O_5I_2$.

show oxidation activity for $\cdot OH$ generation due to the VB potential (+1.43 V vs NHE) was more negative than $E^0(\cdot OH/OH^-) = +1.99$ V vs NHE) [48,49]. Therefore, the photocatalytic oxidation position of $g-C_3N_4/Bi_4O_5I_2$ should be $g-C_3N_4$ -VB rather than $Bi_4O_5I_2$ -VB. This results indicated that Z-scheme mechanism induced the improved photo-induced carrier separation efficiency.

As we known that redox mediator or Z-scheme bridge was very important for photocatalytic Z-scheme mechanism. For examples, noble metal Au and Ag usually acted as Z-scheme bridge in three photocatalytic system [50,51]. And Fe^{3+}/Fe^{2+} and IO_3^-/I^- usually acted as redox mediator for Z-scheme system [52,53]. In $g-C_3N_4/Bi_4O_5I_2$ system, the I 3d XPS spectra (Fig. 9) displayed that the peaks of $g-C_3N_4/Bi_4O_5I_2$ were not symmetrical. Except for the I^- ions at 618.89 eV and 630.36 eV, I_3^- ions (probably deriving from the photocatalytic oxidation of I^- ions) at 620.47 eV and 631.66 eV also appeared. [54,55]. It indicated that I_3^-/I^- redox mediator may play key role for the Indirect Z-Scheme $g-C_3N_4/Bi_4O_5I_2$ photocatalytic system.

Based on the above discussion, the photo-induced electron-hole separation processes for CO_2 conversion was showed in Fig. 10. If the charge transfer mechanism happened (Fig. 10a), the CO_2 conversion reaction (CO was the main product) position of $g-C_3N_4/Bi_4O_5I_2$ should be $g-C_3N_4$ -CB rather than $Bi_4O_5I_2$ -CB. And the H_2O oxidation reaction (O_2 was the main product) position of $g-C_3N_4/Bi_4O_5I_2$ should be $Bi_4O_5I_2$ -VB rather than $g-C_3N_4$ -VB. However, it was impossible for H_2O oxidation reaction on $Bi_4O_5I_2$ -VB (Fig. 5a). So, the photocatalytic CO_2 conversion with CO , CH_4 , O_2 and H_2 generation cannot be enhanced via charge transfer mechanism. And the I_3^-/I^- redox mediator assisted Z-scheme mechanism was more suitable to explain the enhanced activity for CO_2 conversion (Fig. 10b). Under the visible light irradiation, $Bi_4O_5I_2$ and $g-C_3N_4$ were excited. The simultaneous electron transfers pathway ($g-C_3N_4$ -CB $\rightarrow I_3^-/I^- \rightarrow Bi_4O_5I_2$ -VB) enhanced photo-induced electron-hole separation efficiency. At end, $g-C_3N_4/Bi_4O_5I_2$ showed improved photocatalytic activity for CO_2 conversion.

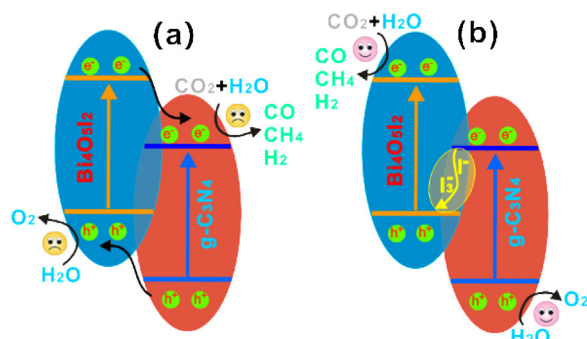


Fig. 10. Photocatalytic enhancement schematic diagram for CO₂ conversion via photo-induced electron–hole separation processes: (a) charge transfer mechanism, and (b) Z-scheme mechanism.

4. Conclusions

In this work, g-C₃N₄/Bi₄O₅I₂ heterojunction samples were prepared and characterized by XRD, FESEM, TEM, DRS and XPS. The photocatalytic CO₂ conversion data showed that an optimal ratio of 1.0 mol% (11.4 wt% of Bi₄O₅I₂) g-C₃N₄/Bi₄O₅I₂ photocatalyst showed the highest photocatalytic activity with 45.6 μmol h⁻¹ g⁻¹ CO generation. Photocurrent and electrochemical impedance spectroscopy revealed that higher photo-induced carrier separation efficiency of g-C₃N₄/Bi₄O₅I₂. Superoxide radical and hydroxyl radical quantification experiments, and I3d XPS spectra of Bi₄O₅I₂ and g-C₃N₄/20-Bi₄O₅I₂ proved the I₃⁻/I⁻ redox mediator assisted Z-scheme mechanism for enhanced photocatalytic CO₂ conversion. In conclusion, this research implied that other bismuth oxyiodide based coupled photocatalysts may also work via Z-scheme mechanism with I₃⁻/I⁻ or IO₃⁻/I⁻ redox mediators assistant.

Acknowledgements

This work was supported by the National Natural Science Foundation of China (No. 51502146, U1404506), Natural Science Foundation of Henan Department of Science & Technology (No. 142102210477), Natural Science Foundation of Henan Department of Education (No. 14A150021), Natural Science Foundation of Nanyang Normal University (No. ZX2014039), Scientific Research Starting Project of SWPU (No.2015QHZ001) and Young Scholars Development Fund of SWPU (No.201499010100).

Appendix A. Supplementary data

Supplementary data associated with this article can be found, in the online version, at <http://dx.doi.org/10.1016/j.apcatb.2016.04.052>.

References

- [1] A.B. Rao, E.S. Rubin, *Environ. Sci. Technol.* 36 (20) (2002) 4467–4475.
- [2] E. Worrell, L. Price, N. Martin, C. Hendriks, L.O. Meida, *Annu. Rev. Energy Environ.* 26 (2001) 303–329.
- [3] J. Reilly, R. Prinn, J. Harnisch, J. Fitzmaurice, H. Jacoby, D. Kicklighter, J. Melillo, P. Stone, A. Sokolov, C. Wang, *Nature* 401 (1999) 549–555.
- [4] M. Santil, P. Moutinho, S. Schwartzman, D. Nepstad, L. Curran, C. Nnobre, *Clim. Change* 71 (2005) 267–276.
- [5] L. Lombardaa, A. Cortib, E. Carnevalea, R. Baciocchic, D. Zingarettic, *Energy Procedia* 4 (2011) 465–472.
- [6] A. Phan, C.J. Doonan, F.J. Uribe-Romo, C.B. Knobler, M.O. Keeffe, O.M. Yaghi, *Acc. Chem. Res.* 43 (1) (2010) 58–67.
- [7] L. Cao, S. Sahu, P. Anilkumar, C.E. Bunker, J. Xu, K.A.S. Fernando, P. Wang, E.A. Gulians, K.N. Tackett, Y.P. Sun, *J. Am. Chem. Soc.* 133 (13) (2011) 4754–4757.
- [8] S. Sato, T. Arai, T. Morikawa, K. Uemura, T.M. Suzuki, H. Tanaka, T. Kajino, *J. Am. Chem. Soc.* 133 (39) (2011) 15240–15243.
- [9] O.K. Varghese, M. Paulose, T.J. LaTempa, C.A. Grimes, *Nano Lett.* 9 (2) (2009) 731–737.

- [10] J. Yu, J. Low, W. Xiao, P. Zhou, M. Jaroniec, *J. Am. Chem. Soc.* 136 (25) (2014) 8839–8842.
- [11] X. Zong, H. Yan, G. Wu, G. Ma, F. Wen, L. Wang, C. Li, *J. Am. Chem. Soc.* 130 (23) (2008) 7176–7177.
- [12] Q. Li, B. Guo, J. Yu, J. Ran, B. Zhang, H. Yan, J.R. Gong, *J. Am. Chem. Soc.* 133 (28) (2011) 10878–10884.
- [13] D. Jiang, Z. Sun, H. Jia, D. Lu, P. Du, *J. Mater. Chem. A* 4 (2016) 675–683.
- [14] G. Liu, P. Niu, L. Yin, H.M. Cheng, *J. Am. Chem. Soc.* 134 (22) (2012) 9070–9073.
- [15] F. Wang, W.K.H. Ng, J.C. Yu, H. Zhu, C. Lia, L. Zhang, Z. Liu, Q. Li, *Appl. Catal. B: Environ.* 111–112 (2012) 409–414.
- [16] X. Wang, K. Maeda, A. Thomas, K. Takanabe, G. Xin, J.M. Carlsson, K. Domen, M. Antonietti, *Nat. Mater.* 8 (2009) 76–80.
- [17] S. Cao, J. Yu, *J. Phys. Chem. Lett.* 5 (12) (2014) 2101–2107.
- [18] S. Chu, Y. Wang, Y. Guo, P. Zhou, H. Yu, L. Luo, F. Kong, Z. Zou, *J. Mater. Chem.* 22 (2012) 15519–15521.
- [19] N. Kijimaa, K. Matanob, M. Saitob, T. Oikawab, T. Konishib, H. Yasudaa, T. Satoa, Y. Yoshimuraa, *Appl. Catal. A: Gen.* 206 (2001) 237–244.
- [20] J. Geng, W.H. Hou, Y.N. Lv, J.J. Zhu, H.Y. Chen, *Inorg. Chem.* 44 (23) (2005) 8503–8509.
- [21] L. Ye, Y. Su, X. Jin, H. Xie, C. Zhang, *Environ. Sci.: Nano* 1 (2014) 90–112.
- [22] H. Cheng, B. Huang, Y. Dai, *Nanoscale* 6 (2014) 2009–2026.
- [23] J. Li, Y. Yu, L. Zhang, *Nanoscale* 6 (2014) 8473–8488.
- [24] L. Ye, L. Zan, L. Tian, T. Peng, J. Zhang, *Chem. Commun.* 47 (2011) 6951–6953.
- [25] J. Jiang, K. Zhao, X. Xiao, L. Zhang, *J. Am. Chem. Soc.* 134 (10) (2012) 4473–4476.
- [26] D. Wu, B. Wang, W. Wang, T. An, G. Li, T.W. Ng, H.Y. Yip, C. Xiong, H.K. Lee, P.K. Wong, *J. Mater. Chem. A* 3 (2015) 15148–15155.
- [27] Z. Ai, W. Ho, S. huncheng Lee, L. Zhang, *Environ. Sci. Technol.* 43 (11) (2009) 4143–4150.
- [28] G. Dong, W. Ho, L. Zhang, *Appl. Catal. B: Environ.* 168 (–169) (2015) 490–496.
- [29] W.L. Huang, Q. Zhu, *J. Comput. Chem.* 30 (2009) 183–190.
- [30] W.L. Huang, Q. Zhu, *Comput. Mater. Sci.* 43 (2008) 1101–1108.
- [31] W.L. Huang, *J. Comput. Chem.* 30 (2009) 1882–1891.
- [32] X. Jin, L. Ye, H. Wang, Y. Su, H. Xie, Z. Zhong, H. Zhang, *Appl. Catal. B: Environ.* 165 (2015) 668–675.
- [33] J. Shang, W. Hao, X. Lv, T. Wang, X. Wang, Y. Du, S. Dou, T. Xie, D. Wang, *J. Wang, ACS Catal.* 4 (3) (2014) 954–961.
- [34] L. Ye, X. Jin, C. Liu, C. Ding, H. Xie, K. H. Chu, P.K. Wong, *Appl. Catal. B: Environ.* 187 (2016) 281–290.
- [35] X. Xiao, C. Xing, G. He, X. Zuo, J. Nan, L. Wang, *Sol. Appl. Catal. B: Environ.* 148–149 (2014) 154–163.
- [36] L. Ye, J. Liu, Z. Jiang, T. Peng, L. Zan, *Appl. Catal. B: Environ.* 142–143 (2013) 1–7.
- [37] L. Ye, J. Liu, C. Gong, L. Tian, T. Peng, L. Zan, *ACS Catal.* 2 (2012) 1677–1683.
- [38] L. Ye, J. Chen, L. Tian, J. Liu, T. Peng, K. Deng, L. Zan, *Appl. Catal. B: Environ.* 130–131 (2013) 1–7.
- [39] N. Tian, Y. Zhang, C. Liu, S. Yu, M. Li, H. Huang, *RSC Adv.* 6 (2016) 10895–10903.
- [40] Y. Peng, P.P. Yu, H.Y. Zhou, A.W. Xu, *New J. Chem.* 39 (2015) 8321–8328.
- [41] K.H. Ji, D.M. Jang, Y.J. Cho, Y. Myung, H.S. Kim, Y. Kim, J. Park, *J. Phys. Chem. C* 113 (2009) 19966–19972.
- [42] L. Ye, X. Jin, X. Ji, C. Liu, Y. Su, H. Xie, C. Liu, *Chem. Eng. J.* 291 (2016) 39–46.
- [43] S.J. Hong, S. Lee, J.S. Jang, J.S. Lee, *Energy Environ. Sci.* 4 (2011) 1781–1787.
- [44] K. Sayama, A. Nomura, T. Arai, T. Sugita, R. Abe, M. Yanagida, T. Oi, Y. Iwasaki, Y. Abe, H. Sugihara, *J. Phys. Chem. B* 110 (23) (2006) 11352–11360.
- [45] H. Li, H. Yu, X. Quan, S. Chen, Y. Zhang, *ACS Appl. Mater. Interfaces* 8 (2016) 2111–2119.
- [46] E. Gao, W. Wang, M. Shang, J. Xu, *Phys. Chem. Chem. Phys.* 13 (2011) 2887–2893.
- [47] D.E. Scaife, *Sol. Energy* 25 (1980) 41–54.
- [48] W. Wang, X. Chen, G. Liu, Z. Shen, D. Xia, P.K. Wong, J.C. Yu, *Appl. Catal. B: Environ.* 176–177 (2015) 444–453.
- [49] M. Mrowetz, W. Balcerski, A.J. Colussi, M.R. Hoffmann, *J. Phys. Chem. B* 108 (45) (2004) 17269–17273.
- [50] H. Tada, T. Mitsui, T. Kiyonaga, T. Akita, K. Tanaka, *Nat. Mater.* 5 (2006) 782–786.
- [51] P. Zhou, J. Yu, M. Jaroniec, *Adv. Mater.* (2014) 4920–4935.
- [52] Y. Sasaki, A. Iwasea, H. Katoa, A. Kudoa, *J. Catal.* 259 (2008) 133–137.
- [53] Y. Mieski, S. Fujiyoshi, T. Gunji, K. Sayama, *Catal. Sci. Technol.* 3 (2013) 1750–1756.
- [54] J.C. Wang, H.C. Yao, Z.Y. Fan, L. Zhang, J.S. Wang, S.Q. Zang, Z.J. Li, *ACS Appl. Mater. Interfaces* 8 (2016) 3765–3775.
- [55] H. Kim, O. Renault, A. Tyurnina, J.P. Simonato, D. Rouchon, D. Mariolle, N. Chevalier, *J. Dijon, Appl. Phys. Lett.* 105 (2014) 011605.